

# Difference Image Analysis of Galactic Microlensing

## I. Data Analysis

C. Alcock<sup>1,2</sup>, R.A. Allsman<sup>3</sup>, D. Alves<sup>1,4</sup>, T.S. Axelrod<sup>5</sup>, A.C. Becker<sup>6</sup>, D.P. Bennett<sup>1,2</sup>,  
K.H. Cook<sup>1,2</sup>, A. J. Drake<sup>5</sup>, K.C. Freeman<sup>5</sup>, K. Griest<sup>2,7</sup>, M.J. Lehner<sup>8</sup>, S.L. Marshall<sup>1,2</sup>,  
D. Minniti<sup>1,13</sup>, B.A. Peterson<sup>5</sup>, M.R. Pratt<sup>9</sup>, P.J. Quinn<sup>10</sup>, C.W. Stubbs<sup>2,5,6</sup>,  
W. Sutherland<sup>11</sup>, A. Tomaney<sup>6</sup>, T. Vandedei<sup>7</sup>, and D.L. Welch<sup>12</sup>

(The MACHO Collaboration)

### ABSTRACT

This is a preliminary report on the application of Difference Image Analysis (DIA) to galactic bulge images. The aim of this analysis is to increase the sensitivity to the detection of gravitational microlensing.

We discuss how the DIA technique simplifies the process of discovering microlensing events by detecting only objects which have variable flux. We illustrate how the DIA technique is not limited to detection of so called “pixel lensing” events, but can also be used to improve photometry for classical microlensing events by removing the effects of blending. We will present a method whereby DIA can be used to reveal the true unblended colours, positions and light curves of microlensing events.

We discuss the need for a technique to obtain the accurate microlensing time scales from blended sources, and present a possible solution to this problem using the existing HST colour magnitude diagrams of the galactic bulge and LMC. The use of such a solution with both classical and pixel microlensing searches is discussed.

We show that one of the major causes of systematic noise in DIA is differential refraction. A technique for removing this systematic by effectively registering images to a common airmass is presented. Improvements to commonly used image differencing techniques are discussed.

---

<sup>1</sup>Lawrence Livermore National Laboratory, Livermore, CA 94550

<sup>2</sup>Center for Particle Astrophysics, University of California, Berkley, CA 94720

<sup>3</sup>Supercomputing Facility, Australian National University, Canberra, ACT 0200, Australia

<sup>4</sup>Department of Physics, University of California, Berkeley, CA 95616

<sup>5</sup>Mount Stromlo and Siding Spring Observatories, Weston Creek, Canberra, ACT 2611, Australia

<sup>6</sup>Department of Astronomy and Physics, University of Washington, Seattle, WA 98195

<sup>7</sup>Department of Physics, University of California, San Diego, CA 92093

<sup>8</sup>Department of Physics, University of Sheffield, Sheffield s3 7RH, UK

<sup>9</sup>Center for Space Research, MIT, Cambridge, MA 02139

<sup>10</sup>European Southern Observatory, Karl Schwarzschild Str. 2, D-85748 Gärching bel München, Germany

<sup>11</sup>Department of Physics, University of Oxford, Oxford OX1 3RH, UK

<sup>12</sup>Department of Physics and Astronomy, McMaster University, Hamilton, ON L8S 4M1, Canada

<sup>13</sup>Departamento de Astronomia, P. Universidad Católica, Casilla 104, Santiago 22, Chile

*Subject headings:* Cosmology: gravitational lensing - methods: data analysis - Galaxy: stellar content; center - stars: brown dwarfs

## 1. INTRODUCTION

The study of microlensing has become well established after a number of groups followed up the ground breaking proposal of Paczyński (1986). Over the past few years well over a hundred events which can only reasonably be attributed to microlensing have been discovered by the MACHO (Alcock et al. 1998a), EROS (Beaulieu et al. 1995), DUO (Alard & Guibert 1997) and OGLE (Paczynski et al. 1994) groups, in their attempt to characterise the nature of the dark matter halo of our galaxy.

Fits to the light curves from microlensing events do not give us a direct measure of the mass of the objects causing the magnification. What they do provide is a measure of the lensing time scale and amplification. The amplification of light from a point source due to microlensing is given by equation 1, where  $u(t)$  can be obtained from equation 2,  $u_{min}$  is the impact parameter in terms of Einstein radii and  $t_{max}$  is the time at which maximum amplification is reached.

$$A(t) = \frac{u^2 + 2}{u(u^2 + 4)^{1/2}} \quad (1)$$

$$u^2(t) = u_{min}^2 + \left( \frac{2(t - t_{max})}{\hat{t}} \right)^2 \quad (2)$$

The time scale  $\hat{t}$  of a microlensing event is set by the time the Einstein ring takes to traverse the source star at velocity  $V_{\perp}$ . The projected size of the Einstein radius  $R_E$  (equation 3), is dependent upon  $D_d$ , the observer-lens distance,  $D_s$ , the source-observer distance,  $D_{ds}$ , the lens source distance, and the lens mass  $M$  (in solar masses).

$$R_E = \sqrt{\frac{4GM}{c^2} \frac{D_d D_{ds}}{D_s}} \quad (3)$$

To uniquely determine the mass of the lens causing any given event, one must determine its distance, the source distance and its transverse velocities relative to our line-of-sight. This is usually not possible. However, for a small number of exotic events where binarity or parallax are found, the degeneracy of  $M$ ,  $D_d/D_s$  and  $V_{\perp}$  (e.g. Alcock et al. 1995) can be broken. One can instead extract the distribution of lens masses by assuming the distribution of lens transverse velocities and distances (Griest 1991). As this is a statistical process, an increase in the number of events

leads to increased accuracy in the determination of lens mass distribution.

The number of events detected in microlensing surveys is limited by the number of stars which it is possible to monitor and the overall detection efficiency. In terms of telescopes, this means such surveys are limited by the size of the field-of-view of the survey telescope and its light gathering power. Limitations to such surveys also come from sampling rate and the seeing. These effects limit the accuracy of the photometry obtained and thus the event detection threshold. To maximise the number of events one naturally chooses to observe fields with the greatest density of stars. This introduces crowding which sets a seeing dependent limiting magnitude for such surveys. To maximise the number of monitored stars one can take an image in the best seeing conditions, where the crowding and sky background levels are at minimum. The detected stars can then be monitored even when the seeing is poor and sky background is high, by transforming the coordinates of stars from the reference image to each subsequent observation. This is the standard approach taken in such surveys.

The use of crowded fields limits the accuracy of photometry. For images with poor seeing conditions, faint stars become immersed in the flux from neighbouring brighter stars. An important consideration when working with such fields, is that only a small fraction of the stars are actually detected. In fact, within each seeing disk there are generally many stars. The determined stellar centroid is actually a flux weighted mean centroid of the seeing disk. Any one of the stars within such a blend can be gravitationally lensed. Blending thus has a major effect on the actual number of stars that are monitored and hence the optical depth to microlensing. Such blending of microlensing events causes an amplification bias in the number of detected events (Bailion et al. 1993, Nemiroff 1994, Han 1997b, Woźniak & Paczyński 1997, Alard 1997). In past analyses such effects have been taken into account statistically (Alcock et al. 1997a), but corrections are difficult to apply on an event by event basis (Han 1997b). In this way the method of monitoring a star field using fixed positions, in some sense, does allow us to monitor some sources which were too faint to have been detected by virtue of their own flux. This does not, however, allow us to detect any microlensing events due to such source stars which are not blended with a neighbouring star or stars bright enough to be de-

tected.

New, large, ground based telescopes are useful in increasing the number and frequency with which star fields can be monitored because of shorter exposure times are required. But such telescopes are still prone to the same intrinsic seeing limits as small telescopes, and thus the same crowding limits of images. The effective seeing can be improved with the use of better observing sites, but this does not resolve the issue of blending completely when many stars are present per square arc second. Attention must be applied to improving the reduction techniques to remove blending effects. Such techniques would also ideally increase the number of events detected by increasing the effective number of stars monitored per image. To achieve both requires a technique which will overcome the crowding in the images and increase the monitored area within each image. With this intent we shall apply difference image analysis (hereafter DIA<sup>14</sup>). This uses a similar technique to that first described by Crofts (1992) and Phillips & Davis (1995).

Lensing events where the source stars are only detectable during microlensing are usually designated ‘pixel lensing’ events. Events where the source star is a resolved are termed ‘classical microlensing’ events (see Gould (1996) and Gould (1997) for full details). The term pixel lensing comes from an analogy with microlensing surveys in M31 (Ansari et al. 1997), where each pixel in this survey represents the sum of hundreds of unresolved stars that may be microlensed. This term is applicable with local microlensing surveys (bulge, LMC) to an extent, since even for the bulge, given arc second seeing, each pixel contains light from a number of stars. In this way we define local pixel lensing events as microlensing events where the sources are not associated with stars we monitor. Furthermore, to remove the ambiguity in what is a pixel lensing event and what is a classical lensing event, we will use the colour and position information available with the DIA technique. The three properties *flux*, *colour*, *position* allow us to make a fairly robust separation between these event types.

In the following sections we will demonstrate how the DIA technique can be used to increase the number and quality of results from microlensing surveys. In the next section we will briefly outline the observational strategy. In §3 we will also discuss how the DIA technique was employed on our set of data and what

improvements to the standard method were made. In §4 we will discuss the relevance of DIA to the issue of blending. In §5 a comparison between PSF photometry and this technique is made. In §6 we outline how to determine source fluxes from the results. In the final section we shall make our concluding remarks. *The light curves and parameters for the microlensing events discovered will be presented in Alcock et al. (1999 paper2).*

## 2. OBSERVATIONS

The MACHO observation database consists of over 70,000 individual observations of the galactic bulge, the LMC and the SMC. The present analysis considers only a single 42' by 42' field (Macho id 108) in the galactic bulge centred at  $\alpha = 18^{\circ}01'20''$ ,  $\delta = -28^{\circ}17'39''$  (*J2000*). Observations were taken on the Mount Stromlo and Siding Spring Observatories' 1.3m Great Melbourne Telescope with the dual-colour (red, blue) wide-field ‘Macho camera’. All bulge observations have 150 second exposure times.

The Macho camera consists of a mosaic of eight  $2k \times 2k$  CCDs (four red, four blue) with  $0.63''$  pixels. Each of the eight CCDs in the Macho camera consists of two amps. Light passing through the telescope is separated into two passbands using a dichroic beam splitter allowing both red and blue images of a field to be taken simultaneously (Marshall et al. 1993).

Observations in this analysis span the dates from the 10th of March 1995 to the 2nd of August 1997 with breaks from the end of October to the beginning of March each year when the bulge is unobservable at Mount Stromlo. Within this observing period 385 observations of the target field were taken. The seeing for the data set varies from  $1.2''$  to  $6.5''$  with a mean of  $2.3''$ . The sky background level in the blue band-pass varies from 1000 to 30000 counts with a mean  $\sim 2600$  counts. Similar levels were observed for red images.

We chose to reject a number of observations from this dataset as good photometry was required to detect microlensing of faint stars. Images with seeing  $\text{FWHM} > 4''$  or blue-band sky background  $> 8000$  ADU were excluded from the reduction. These two cuts removed 42 observations from the data set. As the usable area of a difference images is dependent on the differences in pointing between observations, we also excluded a small number of images where the difference in pointing of the reference and subsequent

<sup>14</sup>This technique is also referred to as image subtraction.

observation was greater than  $25''$ . With this criteria imposed we rejected 19 more observations leaving 324 before reduction was attempted.

### 3. DIFFERENCE IMAGE ANALYSIS

Since the work of Crotts (1992) and Phillips & Davis (1995) there have been a number of applications of DIA type techniques (Tomaney & Crotts 1996, Reiss et al. 1998, Alard & Lupton 1997). These papers show the rapid evolution of the technique to a near optimal case. The implementation of the technique as used here varies in several important aspects to these approaches. So we shall outline our technique, noting the similarities and differences to these applications.

In brief, DIA of our images involves registering a test image to a preselected, high signal-to-noise ratio (hereafter S/N), low airmass, stacked reference image. Next  $\sim 200$  bright, uncrowded, so called PSF stars, are selected to calculate the convolution required to map the template image to the test one. The convolution kernel for this mapping is calculated and applied to the reference. The test image is then photometrically normalised (scaled and offset) to match the convolved reference image. The resultant, registered, convolved and normalised image is then subtracted from the test image. The process is carried out for red and blue passbands, and objects are detected. The positions of these objects are matched in the two colours to separate real objects from spurious ones. The results are then sorted and characterised to separate microlensing events from variable stars.

#### 3.1. Template construction

To perform DIA the first requirement is to have a comparison *reference image* (template) to difference against. To minimise the noise contribution to the final difference images from such a reference image, it is an obvious step to use the highest S/N image. The MACHO project has a database of hundreds of observations of each field taken with the same telescope, under similar observing conditions. This database makes it possible to increase the S/N for a reference image simply by stacking matched images. As the the highest S/N is associated with the best seeing, we choose to degrade the reference image seeing to the test image. Since we require that the reference image has good seeing we can only combine images with good seeing to create it. This considerably lim-

its the number of images we can combine to make the reference image.

To produce this reference image we require the constituent images be taken at low airmass. This is required because the combination must be unaffected by refraction (see section 3.3). We also require that such images do not have high sky backgrounds or sky gradients, so that the combined sky level contributes little noise to the final difference images. Low sky levels allow us to place the lowest possible detection thresholds for pixel lensing events. Care has to be taken selecting images, as even a small residual sky gradient in the combined reference image can affect how well two images are photometrically normalised and thus the quality of the entire set of difference images produced.

Aside from the advantage of an increased S/N in the combined reference image, the process of stacking images has the effect of removing most of the bad pixel regions in the images. Small features in the images due to differences in sky background, transparency, fringing, or poor flatfielding are also reduced.

The airmass, seeing, and sky level selection criteria strongly restrict the number of observations suitable for the reference image combination. Among our  $\sim 324$  observations, only five meet all our requirements.

#### 3.2. Image Registration

The importance of obtaining an accurate registration when performing DIA can not be over emphasised. To accomplish an accurate registration, and to reduce the time required for analysis, we took initial estimates for the geometric alignment transformations from a database produced when each image was PSF photometered. These transformations were applied to some hundreds of bright stars spread across each image. The transformed positions of these stars were then used as starting points where more accurate centroid positions were determined. The initial centroid positions were found to be good to within a pixel ( $0.63''$ ). Such accuracy means we do not have little possibility of centering on the wrong star. These new centroid positions for the stars in the test and reference images were used in the IRAF tasks *geomap* and *geotran* to register the image. The use of a large number of stars allowed us to determine an accurate mapping between the images where small rotations, translations and distortions may be present.

The images were initial registered with a simple

linear transformation on a  $10' \times 10'$  scale. However, we found this was inadequate for the alignment accuracy we require from this technique ( $< 0.1''$ ). This is likely to be caused by distortions between images, due to small effects such as differences in telescope flexure with zenith distance. For the final analysis we have used a fifth order Chebyshev geometric transformation mapping for blue images, and a third order mapping for red images (where differential refraction effects are not so important, see next section).

The pointing accuracy of the Great Melbourne Telescope is good, with the standard deviation in offset between successive observations of a field being approximately  $10''$ . For difference images this results in the loss of a very small amount of data at the edges of the images where the observation and reference image do not overlap.

The registration process is accurate to about 0.07 pixels ( $\sim 45$  milli-arc seconds) on average (c.f. Reiss et al. 1998,  $\sim 0.3''$ ). We believe our accuracy is due to the inclusion of higher order transformation terms and the large number of stars used to constrain the fit. To show the importance of accurate image registration we present figure 1. In this figure we approximate a standard stellar profile as a Gaussian. Using the average seeing of  $\sim 2.5''$  and an offset between two stellar profiles of  $0.3''$ , we expect the average residual (as seen perpendicular to the offset direction) to have the form of the long dashed line given. For our average registration accuracy ( $0.07''$ ) the stellar and residual profiles are given by the short dashed lines. For this figure we did not include the effects of pixelisation or photon noise, as this makes little difference to the observed effect.

### 3.3. Differential Refraction Corrections

The first mention of the deleterious effects of atmospheric refraction on difference images was made by Tomaney and Crotts (1996). They stressed that, for broad-band filters, the centroid position of a star is dependent upon the airmass of the observation. The phenomenon is well known in astrometry and has the effect of increasingly elongating the PSF with airmass. For observations taken at different airmasses this leads to poor subtraction. By poor subtraction we mean that the systematic noise contribution from the refraction effect is obvious in the images. The presence of this is revealed by a significant residual flux remaining in the difference image.

To better understand the refraction effect, one must understand that every star within the frame has a centroid position which is dependent upon its colour and the airmass at which it is observed (Gubler & Tytler 1998). If all the stars were of the same colour then the registration process alone would compensate for the shift in centroid position with airmass, and the difference image would only be effected by the elongation. However, this is not the case. The image registration is in reality a registration to the average colour of the stars. We suggest that, two images observed through broad-band filters at blue wavelengths and at moderately different airmasses, can not be geometrically registered accurately enough to provide truly photon noise limited difference images. However, we further suggest that, if each star were to be registered separately we could come close to this. With this realisation in mind, Tomaney and Crotts (1996) proposed that ‘There was no easy way to compensate for this, particularly without knowledge of the precise position and colour of all detected and undetected (blended) stars’. Similar effects have also been noted by Melchior et al. (1996) who believed that atmospheric dispersion affected their pixel lensing search in M31. This effect was given to be between  $0.73''$  to  $2.75''$  in the extremes of their blue filter. With this result it is easy to understand the importance such an effect could have. However, such a large effect does not occur in our DIA analysis, even in the worst case, as the first order refraction effect is an offset of all stars in an observation. This offset is taken out in the registration process. It is only the smaller second order effects, caused by differences in star colour which cause differential refraction offsets. The corrections for these effects are in the order of tenths of an arc second at blue band wavelengths and so are still appreciable.

To correct for differential refraction the following approach has been taken. As a first approximation, the effective temperature for any given star can be associated with a colour. We know the position of the centroid of a star is dependent upon the colour of the star and the airmass. So if one knows the airmass, the colour and the observation parallactic angle it should be possible to determine the change to the stellar flux distribution with airmass and parallactic angle.

To determine the degree of change we first modelled our galactic bulge stars based on Bessell’s (1998) tabulated colour-temperature relations. We then assumed a blackbody spectrum approximation for these

stars with no blanketing or spectral features.

These spectra were then integrated within the MACHO Camera's blue( $B_m$ ) and red( $R_m$ ) passband responses to find the average centroid wavelength associated with a given star colour. The V-R colours for Bessell's (1998) tabulated stars were transformed to Macho  $R_m$  and  $B_m$  colours using the results of Alves (1998). A star of a given colour can thus be related to this *centroid wavelength*.

$$R_0 = \frac{(n^2 - 1)}{2n^2} \quad (4)$$

$$R = z_t - z_a \quad (5)$$

$$R \approx R_0 \tan z_a - 0''.067 \tan^3 z_a \quad (6)$$

The refraction of light at a given wavelength, temperature and airmass is given by Filippenko (1982). Using the equations in Filippenko (1982) and equation 4 one may determine the constant of refraction, where  $n$  is the refractive index of air. The degree of refraction is given by equation 5, where  $z_t$  is the true zenith position and  $z_a$  the apparent. Under normal temperature and pressure conditions (15°C, 760 mm Hg) this reduces to equation 6, and  $R_0$  becomes 58.3''.

The positional shift of the centroid of the star is associated its average blackbody wavelength. For a star of known colour the centroid shift can be obtained. The offset in the centroid positions for the model stars are given in figure 2 for three values of airmass. To make use of this information, one needs to know the colour of each star and must be able to shift its centroid in proportion to this colour. This task sounds more daunting than it really is. In fact, this can easily be achieved (at least approximately), for two images taken at a known airmass in the following way. Using the IRAF tasks *geomap* and *geotran*, it is possible to map two images of different sizes, orientations and even geometric distortions onto each other. We used these tasks to map the images from the two passbands of the MACHO camera onto each other. These mapped images were then used to form a quotient image which, after sky background subtraction, can serve as a colour map of each pixel in the field. However, as the centroid wavelengths of each star within the two passbands varies with airmass, one must calculate this quotient near unit airmass not to have a colour map which is affected by refraction.

To find the relationship between the pixel values of our colour map, and the V-R colours of the stars present in the colour map, a simple calibration is carried out. Having performed photometry on the individual images in the colour map, one can associate a  $B_m - R_m$  and hence, a V-R colour, with a quotient image pixel value. We thus have a V-R colour for every pixel within the image (except for saturated or bad pixels). The relationship between the measured  $B_m - R_m$  photometry values and the associated colour map pixel value is given in figure 3. The relationship is quite strong for most stars. A small number of points are scattered due to stars being blended with neighbours.

As the degree of refraction is wavelength dependent it is in fact only necessary for us to apply our corrections to images taken through the blue passband. In red passband the centroid offset is less than one quarter ( $< 0.1''$ ) that of the blue passband (see figure 4).

The final result is that each blue image pixel value in the reference image was interpolated based on the calibrated colour map pixel values, the airmass of the observation relative to the reference image, and the parallactic angle of the observation. The flux corrections were carried out while imposing a condition of flux conservation within the image. We interpolated the flux in the reference image rather than in each observation as, for most observation it is not possible to make a colour map for these due to first order of refraction effects. Colour maps made with individual observations would have much lower S/N and CCD defects.

The results from this reduction were used as an initial estimate, as it was known that the results for the differential refraction offsets would be dependent on the assumptions about the model stars (smooth blackbody emission) and the uncertainty in the form of the Macho blue band response function. This estimate was improved by differencing a number of images taken at a range of airmasses to obtain a semi-empirical result for the offset required with colour and airmass (relative to the reference image).

The scale of our corrections can be seen in figure 5. On the left is a difference image where the effects of differential refraction have not been removed. On the right the differential refraction corrected images is shown. The test image used in producing these difference images is at an airmass of 2.4 (approximately the airmass limit imposed on these observations). The

template airmass is 1.01, so the corrections applied in this case are quite large. However, the same degree of differential refraction effects is observed at much lower airmasses when the seeing quality of the test image is good. The residual is highly dependent on seeing, with the best seeing images being affected much more because of the steepness of the stellar profile.

The calibrated differential refraction corrections for the blue passband of the Macho camera, as a function of airmass and colour, are given by:

$$S = 0.29 \times [\tan(\arccos(1/A_R)) - \tan(\arccos(1/A_T))] \quad (7)$$

$$O = S \times (C - 0.6) \quad (8)$$

$S$  is related to the scale of the offset for airmasses  $A_R$  and  $A_T$ , of the reference and test images respectively.  $O$  is the offset to apply to a given pixel (in arc seconds) of V-R colour  $C$ . This process compensates for the shift in the stars centroid position. It does not compensate for the dispersion of the PSF with airmass. However, we believe this effect to be quite small and for our purposes ignorable.

### 3.4. PSF Matching

The Point Spread Function (PSF) shape of two images taken at different times is never exactly the same. If we were to match the photometric conditions of a reference and test image and then difference the images, we would not expect to obtain a resulting image without systematic noise. What one would invariably find from such a process is that at the position of each star there would be systematic residuals. The degree and structure of these residuals would be dependent upon the form of the spatial difference between the PSFs. To achieve the best difference images one has to match the form of the PSFs. As we mentioned earlier, the template is constructed so that it has high S/N and seeing similar to the best observation<sup>15</sup>. To match the PSFs we degrade the reference images' seeing to match that of the test observation.

The PSF-matching process is based on the fact that it is theoretically possible to match the profiles of stars observed under two different sets of conditions, with a simple convolution of the form given by equation (9). Here  $r$  characterises the flux distribution

of a star in good (better) seeing and  $t$  that in poor seeing,  $k$  is the convolution kernel. A convolution in real space is equivalent to a multiplication in Fourier space. Therefore, in principle, the Fourier Transform of the kernel required to match the good seeing (reference) image to the poor seeing (test) image, should be the quotient of the Fourier Transforms of the star. The Inverse Fourier Transform recovers the required matching kernel (equation 10).

$$t(x, y, z) = r(x, y, z) * k(x, y, z) \quad (9)$$

$$k = IFT\left(\frac{FT(t)}{FT(r)}\right) \quad (10)$$

In reality a division of these Fourier Transforms is very sensitive to the high frequency, low power, noise component. This leads to a poor match of the images. To fix this one can use the fact that, the PSF of a star is roughly Gaussian, and the Fourier Transformation of a Gaussian is a Gaussian. We can then select a level in Fourier space below which the noise component is dominant, and replace this with a Gaussian fit to the FT (Ciardullo 1990). This method is not always useful because in many cases the wings of the FT are not well modelled by a Gaussian.

To determine the best convolution kernel, the highest S/N, least blended PSF stars are required. We thus need these *PSF stars* to be unblended with neighbouring stars in the bulge where effectively all stars are blended. Blended stars must be removed from those used in determining the PSF.

This situation was overcome by producing a list of a couple of hundred bright stars on a given image. Stars were culled from the list based on the relative proximity and brightness of neighbouring stars. Blending of bright stars can in part be determined from the shape of the PSF of each star. We thus selected stars based on their ellipticity, position angle, FWHM and moment. The remaining stars were then combined to form a generalised PSF profile for the image.

A further complication to the ideal case arises from the fact that the form of the PSF varies across a frame because of poor focussing, telescope flexure and temperature dependent effects (see Tomaney & Crotts 1996). If a single star is used to PSF-match an entire image, the systematic noise in the difference image increases the further one gets from that star. A solution to this is to split the image into sub-rasters and use

<sup>15</sup>All observations are well sampled with minimum FWHM of  $\sim 2.8$  pixels.



a local PSF to match the sub-regions of the image. The sub-rasters can then be mosaiced back together to reform the image. Thankfully the magnitude of the PSF variation for our observations is small, with modest sized effects due to differences only being seen on the scale of  $500 \times 500$  pixels (or  $5' \times 5'$ ).

The actual matching of PSFs is accomplished using the IRAF task *PSFmatch*. This task is similar to the implementation used by Riess et al. (1998) but has been updated to include new features. The convolution kernel is determined for sub-rasters  $500 \times 500$  and each is convolved separately then mosaiced to form  $1k \times 1k$  images. The entire observation field of the MACHO camera is  $4k \times 4k$  per bandpass but larger images were not made because of problems with matching such as the scaling, colour terms, differences in bias levels and gain in the different CCDs (Reiss et al. 1998).

The process of replacing the noise with the Gaussian fit is not regarded as the optimal approach because of there are real differences between the PSF shape and a Gaussian. To improve the difference image quality we characterise the residuals in the difference image and remove them. This is accomplished in the following manner. By stacking sub-rasters of the difference image at the positions where the PSF stars were in the reference image, we determined the median systematic residual at each pixel of the PSF profile. This stacked residual image characterises the real deviations of the PSF shape from that used in the matching process. This image was then scaled and subtracted from our test image PSF. We finally had an essentially empirical PSF and no need to replace the wings of the FT. The convolution kernel is now recalculated without the Gaussian replacement and the difference images recalculated. This final PSF appeared to give the best possible subtraction with the available stellar information. This step was found to reduce the systematic residuals by a factor of  $\sim 2$  in most cases. The final resulting difference images had an average systematic noise component of  $\sim 1.3\%$  in both colours, with some images having less than  $0.5\%$ .

### 3.5. Photometric Scaling

A standard approach to matching reference and test images photometrically is to make a linear fit to the pixel values for a single star found on both images (Reiss et al. 1998). The test image is then scaled and offset using the fit values. We refer to this as a single point calibration. Another approach is to use

photometry taken on a matched set of stars in the two images and scale the image based on this information. In our analysis we apply this second approach which we believe is superior.

The single point technique has the advantage that it uses all the pixel information for this region. However, it suffers from the fact that most of the pixels have a low S/N ratio as they come from the wings or background around a star. As there are very few pixels with high S/N, the fitted slope can be skewed by the pixels near the background noise limit.

An important consideration when matching images is that the two images were probably taken under different seeing conditions. Although the PSF profiles have already been matched, real images can have gradients in sky brightness and transmission. Sky brightness gradients can often be attributed to the proximity of the observed field to the moon, and naturally are dependent on its phase. Differences in the transmission come with airmass, cloud cover and dust extinction. Such differences in sensitivity can also be caused by problems with the flatfielding.

A single point calibration can not compensate for the presence of these spatial variations. However, this can easily be achieved by performing photometry on matched pairs of stars across the two images. This photometry gives a scaling factor (which represents changes in transmission), and an offset term (which represent the change in the sky brightness), for each position where the photometry was performed. To deal with the possibility of gradients we fit a low order polynomial<sup>16</sup> to the scaling and offset terms and determine a transformation for each pixel in the test image. Such a method requires a large number of points within the image to constrain the fit. This is not a problem as there are many thousands of stars per square arc minute in bulge fields.

The photometric scaling we used was always applied to the test image so that images were always registered to the same reference image. In this way no correction was required for transmission differences with airmass.

### 3.6. Object Detection

The fully matched images were differenced to reveal objects whose flux rate has varied in some way. The images were then searched for these sources.

<sup>16</sup>We expect variations in sky level and transmission to be relatively smooth.

Variable stars are detected as positive or negative sources as they became brighter and fainter than they were in the reference image. However, microlensing events and asteroids generally only appear as positive excursions from the reference image baseline<sup>17</sup>.

For source detection we applied a purpose written programme. We felt this approach was necessary as the nature of the noise distribution is unlike that in other images. The fundamental difference is that the noise varies from pixel to pixel even though there is no signal. This is due to the photon noise of the subtracted stars. With such a programme we search for positive and negative source simultaneously.

To detect objects we would ideally would like to know the noise at each point in the image. To determine this we simultaneously examine the reference and difference images. The significance of each detection is accessed based on its S/N. We calculate the noise at each source position using the flux in the reference image and systematics from the difference image. The various noise components (photon, readout, systematic) are well characterised in the reduction and used to provide a position dependent noise threshold for the difference image. The photon noise of the test image dominates for faint objects whereas for brighter objects the systematic noise from the difference image becomes important. As the seeing in our data set is always greater than two pixels, we choose to determine the signal in a  $3 \times 3$  pixel box at every point in the image. The amount of signal in this box is compared with the noise expected for the same pixels in the reference image. Results with a  $S/N > 3$  were written to a file along with other noise parameters such as the systematic and readout noise of the difference image.

The detection process is carried out with images from both passbands. The positions of objects found in the two colours are taken to be matched if they were within  $1''$ . This colour match provides a strong constraint which separates the *real* objects from the large number of detections due to cosmic rays, bad pixels and saturation effects.

Candidate objects which pass these selection criteria were then checked against those obtained in previous reductions of the field. If no match is found, these new results were added to the database of object positions. If a result has previously been detected, the

number of detections for this object is incremented. This provides us with an extra parameter in characterising the nature of the object. Objects detected most often can usually be attributed to variable stars, whereas other detections can be due to asteroids or microlensing events.

### 3.7. Light Curves

Aperture photometry is performed on the red and blue difference images at the sources positions. We feel PSF photometry is unnecessary as the difference images are no longer crowded with non-variable objects. The noise is obtained from the initial images as noted in the detection strategy. With this photometry we produce a database which is used to produce difference-flux light curves for microlensing event detection.

These positions where photometry is performed are independent of whether there is flux at this position in the reference image or not. This varies from the traditional approach which has been to only follow up stars detected in the template (reference) image. With this technique we are searching among a database of variables for microlensing rather than among a database of all objects. The number of light curves which require scrutiny is thus around a factor of twenty less than the number of stars detected in the reference image. The removal of the positional dependence gives us greater sensitivity to detecting microlensing of stars which were either too faint or too blended to be resolved in the reference image. This effectively provides us with a larger search area and a greater number of monitored stars.

## 4. BLENDING

Firstly, let us define what we mean by blending. This is the case in which two or more stars are located within a few pixels of each other and the seeing disk is greater than a few pixels. Such blending is dependent on seeing and masks the true baseline flux of microlensing sources. In this analysis, we are not concerned with the case where the lens in a microlensing event emits flux which is blended with the flux from the source. In this case the flux of the lens is not amplified and such blending is generally negligible for stars with masses consistent with microlensing results. The colour shifts associated with this type of blending usually can not be detected with the present level of photometry (Buchalter et al. 1996). This case

<sup>17</sup>It is possible for microlensing events to appear with negative flux if they were amplified in the combined reference images.

is also generally inseparable from blending with objects which are not the sources. We are also unconcerned with blending where the source is in a binary association. Here the sources can be blended within the Einstein radius, but this constitutes a small number of events (Griest & Hu 1992, Dominik 1998) and in many cases one can detect such events from the microlensing light curve.

The presence of the apparent blending of the stars monitored in microlensing surveys has been known for some time (Nemiroff 1994), and is inherent in the fact that the fields used for microlensing searches are crowded. These fields were chosen because of the large number of stars that could be monitored at one time. Crowding is demonstrated by figure 6, where the number of stars blended within the seeing disk of the bright stars can be clearly seen.

The main effect of the blending is that we do not know the true source flux for most events. If such events are fitted as unblended sources, the amplitudes of the events and the event time scales are underestimated, and the number of stars monitored is under-estimated (Han 1997a, Woźniak & Paczyński 1997). The overall consequence, if blending is unaccounted for, is that  $\sim 40\%$  of events towards the bulge are affected by amplification bias and thus the determined optical depth can be overestimated by a factor of  $\approx 1.3 - 2.4$  (Han 1997a). The blending effect is therefore, a major factor in the determination of the true optical depth to microlensing toward the galactic bulge, LMC, SMC and M31. Statistical corrections have been made for the LMC and the bulge optical depths (Alcock et al. 1997a, Alcock et al. 1997b), but corrections are really required on an event by event basis. One way to bypass the effects of blending would be to have HST images of all the events. With this approach we could resolve the source star and obtain an unblended source flux. Unfortunately a large number of hours of HST time are needed to perform this (Han 1997b). We note, however, we do have HST observations of microlensing sources for a number of important events.

To determine the blending in the case of classical microlensing, one must attempt to fit the light curves to find the unblended, blended, flux component of the source baseline flux. In this regard Woźniak & Paczyński (1997) noted that one can only determine the blend fraction, with the present accuracy of photometry, when the impact parameter is small,  $u_{min} < 0.3$ . This is the case in only a small percentage of

events. The situation is not quite the same with DIA as we have different information. We shall outline this in the next section. In short, instead of the colour, centroid and light curve of the blend, we have the colour and centroid of the source and the light curve of the source amplification.

## 5. DIA VERSUS PSF PHOTOMETRY

Our usual technique to detect microlensing is to perform PSF photometry simultaneously at fixed positions in two passbands. With our DIA technique, photometry is carried out at the end of the reduction process, at positions where excess flux was detected at some time during the reduction.

The main advantage of using traditional PSF photometry over DIA comes when dealing with fields where the stellar profiles are not blended together. In such situations the determination of the PSF from a few stars is relatively simple. PSF photometry, unlike DIA photometry, is not subject to either the addition of photon noise via the differencing process or the systematics introduced in the image alignment and matching processes.

One common belief about difference image techniques, is that it is not as powerful at constraining microlensing as standard PSF photometry because it does not give a baseline flux. This is not the case. For classical microlensing events, photometry can simply be done once on the reference image to determine the baseline flux. In our present method of analysis this image has a higher S/N than any individual image in the data set, and has the best seeing and a well defined PSF. The photometry baseline determined from this frame can simply be added to the individual difference frame photometry to provide the same flux baseline as the standard PSF photometry. However, this source flux baseline can still be blended as in the PSF case.

To produce difference images with the lowest possible systematic noise, the input images must be accurately photometrically matched. If the difference image has only a small contribution from systematics, then we know that the images were accurately matched photometrically. To perform PSF photometry we have to make corrections for airmass and differences in transmission between observations.

In figure 7 we show the photometry performed on an object with DIA and with PSF photometry using the same set of images. A quite dramatic im-

provement in the photometry is seen. Proof that this demonstrates a real improvement in photometry is evident from the microlensing fit residuals shown on the same figure. Although only one colour is shown, data points from both passbands were consistent within the uncertainties presented. The improvement in photometry comes partly from the fact that the source in this event is highly blended with a neighbouring bright star. With DIA the nearby non-variable star is more accurately removed than with the standard PSF photometry. The PSF photometry is also dependent on how well the centroid positions of the stars were initially determined in the template image. On the other hand, DIA is dependent on how well the entire frame was aligned. The flux from unlensed blended stars is removed accurately even when unresolved with DIA. Such an improvement in the baselines of microlensing events are required for the detection of the subtle effects of parallax and the presence of binary sources.

Another advantage of the DIA scheme over PSF photometry is that the difference flux represents the true colour of a microlensing event. This colour information is useful in deciding whether an event is blended or not. Furthermore, all difference images are matched spatially and photometrically. Thus we can stack images over the period where the microlensed flux was above the background noise. The stacked difference image can then be used to determine the source star colour more accurately.

The present solution to the problem of blending in the PSF photometry is to use the fact that the measured flux within a microlensing event can be represented by equations 11 and 12 (Alcock et al. 1997a),

$$f_R(t) = f_{uR} + A(t)f_{sR} \quad (11)$$

$$f_B(t) = f_{uB} + A(t)f_{sB} \quad (12)$$

where  $f_{uR}$  and  $f_{uB}$  are the fluxes of the unlensed blended sources and  $f_{sR}$ ,  $f_{sB}$  are the baseline fluxes of the lensed star. All of these terms must be found from the microlensing fits. The major problem with this approach is that, even if we know the true colour of the source, we do not know its true brightness. For bright, well covered microlensing events, source fluxes can be found. However, when uncertainties of  $> 1\%$  are associated with the photometry, the fit is practically degenerate with respect to the unlensed flux component (see Woźniak & Paczyński 1997). This

means we can not accurately determine the value of the amplification for a large number of events.

In figure 8 we show three models of the amplitude of a microlensing event with different values of the lensing parameters corresponding to different values of source flux (given in table 1). In the top panel there are three curves which are almost indistinguishable. In the lower panel we plot the difference between the dashed curves and the solid one. One can see that even for such large differences in source flux, hence lensing amplitude, differences of less than a couple of percent occur in the form of the difference in curve shape. The difference between the curves increases only slowly as one moves away from the true values. This predicament is improved greatly with photometry taken in two or more colours because of the extra leverage this gives.

For DIA the flux in the two band-passes is given simply by equations 13 and 14. Here we do not have blending to consider so there is no unlensed flux term. The difference fluxes in the two passbands are given by  $f_{RD}(t)$  and  $f_{BD}(t)$ . The constant  $C$  is the ratio of blue to red flux which can be obtained from the colour of the source.

$$f_{RD}(t) = (A(t) - 1)f_{sR} \quad (13)$$

$$f_{BD}(t) = (A(t) - 1)Cf_{sR} \quad (14)$$

For this situation we only need to be able to measure the baseline flux in one colour to determine the amplitude, since  $Cf_{sR} \equiv f_{sB}$ . If this is not possible, the accuracy of the determination of the amplitude suffers from the same problems as the PSF photometry. For cases where we can not determine the baseline flux (pixel lensing), it should be possible to estimate this quantity statistically.

## 6. SOURCE FLUXES

The case of determining the source flux with pixel microlensing is similar to the case of determining the blending for classical microlensing. In both situations we do not know the initial source flux. The standard way to determine the true amplitude of microlensing events is to use the shape of the light curve. The accurate determination of the source flux requires well sampled light curves with small percentage errors. In many cases the present data does not meet this requirement.

With pixel lensing the source star of the event is initially unresolved and the S/N is generally low. The task of determining an accurate source flux can be impossible in many cases. However, from the reference image we can determine an upper limit to this flux. In such cases, as for DIA of classical microlensing events, we still have an accurate position and colour for the source. With this colour (and the associated uncertainties), the HST luminosity function of the bulge (Holtzman et al. 1998), the upper limit of source flux, and the shape of the light curve, one can determine the probability distribution associated with the source flux for each pixel lensing event. This source flux probability distribution and the light curve shape can be used to give the distribution of  $\hat{t}$  for each event. The combination of these  $\hat{t}$  distributions gives us an overall distribution of  $\hat{t}$  from which the lens mass distribution can be extracted in the traditional way (Griest 1991).

For classical microlensing events where the sources are faint and the amplifications are moderate, the associated photometry errors are typically greater than a few percent. Typically for these events, as for pixel lensing events, we can not accurately determine the amount of unblended lensed light because of blending. In order to use these events when determining the microlensing optical depth, one approach could be to use the same technique as outlined above for pixel lensing. This would help to constrain a large number of classical events. Indeed this approach is desirable when we consider the effect of blending on measured optical depth.

Aside from the aspects mentioned above, we note that, Griest and Hu (1992) and Dominik (1998) found that it was possible that galactic binary sources are fitted well with a single source with blending. As DIA does not suffer from blending this caveat is removed and the light curves should thus readily give unbiased results for binary sources.

Again we remind the reader to the results of this analysis can be found in paper 2.

## 7. SUMMARY

We have outlined a detailed approach to the DIA scheme. A method of using multiple PSFs to addresses the shortfalls of matching images with a single PSF was discussed. We noted how gradients in transmission and sky level across an image can be important when producing difference images. A solution

using a spatially dependent photometric offsets and scaling was outlined. A method for reducing difference images noise by combining observations to form the reference image was presented.

The importance of using an accurate image registration was stressed. The effect of differential refraction on difference images has been examined and is shown to be crucial. A method for compensating for differential refraction by offsetting stars relative to their colours was presented.

A new method for determining the distribution of event time scales was discussed. This method would use existing HST colour-magnitude diagrams to determine the distribution of possible event sources with colour. The colours of events determined with DIA would then be used to determine a distribution of possible  $\hat{t}$  values for each event. These would then be combined to determine the overall distribution of  $\hat{t}$  values. From this lens mass distribution can be found in the usual way.

We have demonstrated how the DIA photometry can make a large improvement in the quality of light curves over PSF photometry because of blending. We discussed how there are fundamental differences between results from PSF and DIA photometry. Difference images naturally provide unblended colours and centroid positions and lightcurves for microlensing events, while PSF results are usually blended to some extent.

We are grateful for the skilled support by the technical staff at Mount Stromlo Observatory. Work at Lawrence Livermore National Laboratory is supported by DOE contract W7405-ENG-48. Work at the center for Particle Astrophysics at the University of California, Berkeley is supported by NSF grants AST 88-09616 and AST 91-20005. Work at Mount Stromlo and Siding Spring Observatories is supported by the Australian Department of Industry, Technology and Regional Development. Work at Ohio State University is supported in part by grant AST 94-20746 from the NSF. W. J. S. is supported by a PPARC Advanced Fellowship. K. G. is grateful for support from DOE, Sloan, and Cottrell awards. C. W. S. is grateful for support from the Sloan, Packard and Seaver Foundations. This work was carried out by A.J.D. in partial fulfilment of the requirements for the degree of PhD at ANU.

## REFERENCES

- Alard, C. 1997, A&A, 321, 424
- Alard, C., & Lupton, R. H. 1997, astro-ph 9712287
- Alard, C., & Guibert, J. 1997, A&A, 326, 1
- Alcock, C., et al. 1995, ApJ, 454, L125
- Alcock, C., et al. 1997a, ApJ, 486, 697
- Alcock, C., et al. 1997b, ApJ, 479, 119
- Alcock, C., et al. 1998a, ApJ, 492, 190
- Alcock, C., et al. 1998b, ApJ, 494, 396
- Alcock, C., et al., 1999, In preparation
- Alves, D. 1998, PhD thesis
- Ansari, R. et al. 1997, A&A, 324, 843
- Bailion, P., et al. 1993, A&A, 277, 1
- Beaulieu, J. P., et al. 1995, A&A, 299, 168
- Bessell, M., 1998, private communication
- Buchalter, A., et al. 1996, ApJ, 469, 676
- Ciardullo, R., Tamblyn, P., & Phillips, A. C. 1990, PASP, 102, 1113
- Crotts, A. 1992, ApJ, 399, L43
- Dominik, M. 1998, astro-ph 9801119
- Filippenko, A. 1982, PASP, 94, 715
- Gould, A. 1996, ApJ, 470, 201
- Gould, A. 1997, ApJ, 480, 188
- Gubler, J., & Tytler, D. 1998, PASP, 110, 738
- Griest, K. 1991, ApJ, 366, 412
- Griest, K., & Hu, W. 1992, ApJ, 397, 362
- Han, C. 1997a, ApJ, 484, 555
- Han, C. 1997b, ApJ, 490, 51
- Holtzman, J. A., et al. 1998, AJ, 115, 1946
- Marshall, S., et al. 1993, BAAS, 182, 71.03
- Melchior, A. -L., et al. 1998, astro-ph 9712236
- Nemiroff, R. J. 1994, AJ, 435, 682
- Paczynski, B. 1986, ApJ, 304, 1
- Paczynski, B., et al. 1994, A&AS, 187, 14.07
- Phillips, A. C., & Davis, L. E. 1995, ASP conf. series, 77, Astronomical Data Analysis Software and Systems IV, ed. R. A. Shaw et al., 297
- Reiss, D. J., et al. 1998, AJ, 115, 26
- Tomaney, A. B., & Crotts, A. P. 1996, AJ, 112, 2872
- Woźniak, P., & Paczyński, B. 1997, ApJ, 487, 55

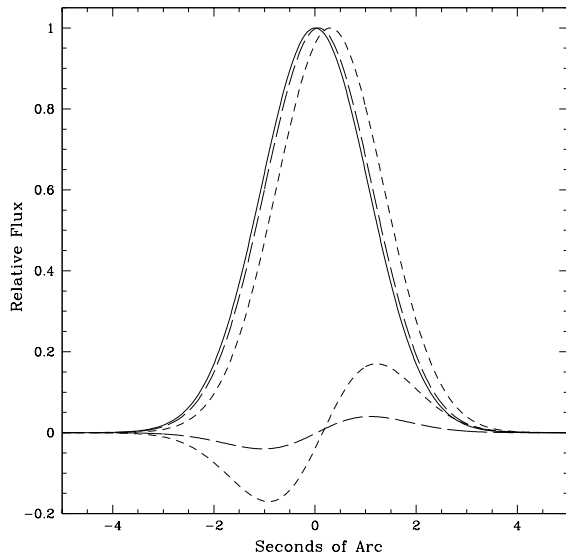


Fig. 1.— Gaussian modelled profiles of three stars and the residuals when the two dashed profiles are differenced against the solid one. The short dashed lines corresponds to a centroid offset of  $0.3''$ . The long dashed lines corresponds to an offset of  $0.07''$ , the average offset of our data.

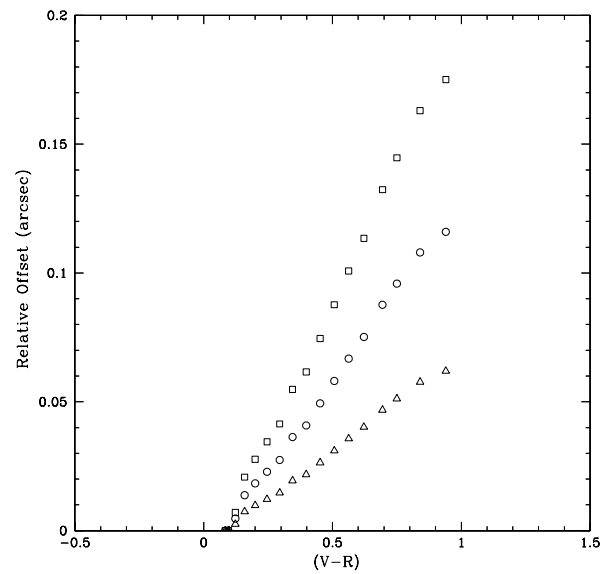


Fig. 2.— Predicted differential refraction offsets between stellar centroids for a range of star colours and airmasses. Offsets are simulated for three airmasses relative to a reference airmass of 1.01 and V-R colour of zero. The three airmass values are 1.9 (squares), 1.5 (circles) and 1.2 (triangles). Results are for the MACHO Blue ( $B_m$ ) passband.

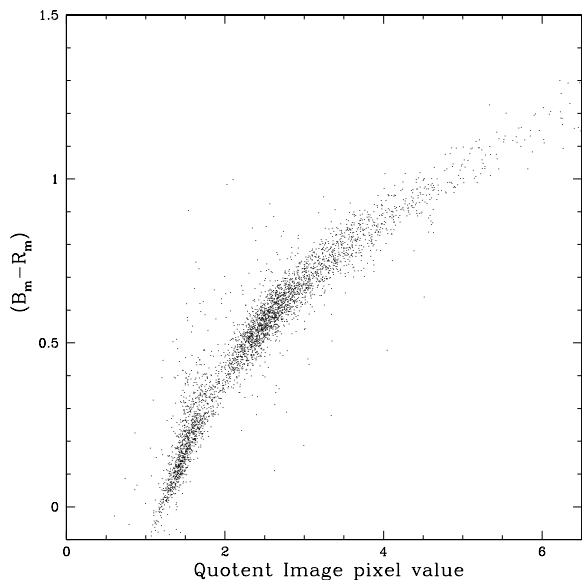


Fig. 3.— The relationship between pixel values in the red divided by blue quotient image (colour map) and the standard MACHO passband colours  $B_m$  and  $R_m$ . Values are used to determine and correct for offsets cause by differential refraction for each pixel(star) in the image.

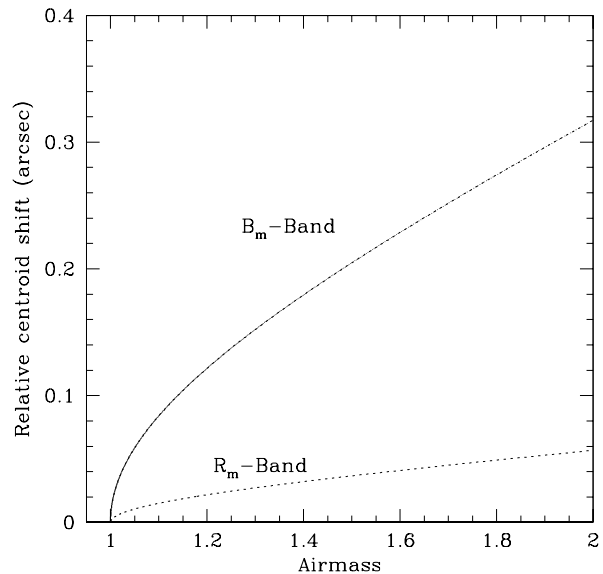


Fig. 4.— Difference in the offset induced by differential refraction as a function of airmass, for a 5K (model) star and a 10K (model) star. The two MACHO Camera passbands  $B_m$  and  $R_m$  are shown. Offsets in the blue passband are much bigger than the red because of the strong wavelength dependence of refraction.

Fig. 5.— The effect of differential refraction on difference images. Left image is a difference image without applying any correction for differential refraction effects. The right image is the same image with our correction technique applied. The scale of the noise structures is much reduced although not completely removed. The two images are  $100'' \times 100''$ . The residual object in the centre is due to a variable star

Fig. 6.— Blending. Left: the position of an microlensing event (arrowed) in an  $11'' \times 11''$  ground based image Macho database image. Right: a drizzled HST image of the same region with reference stars (A - E) to approximately the same scale. Note the number of objects blended within the ground based images seeing disk. This result comes from an event in the LMC where the crowding is similar to the images analysed in this analysis.



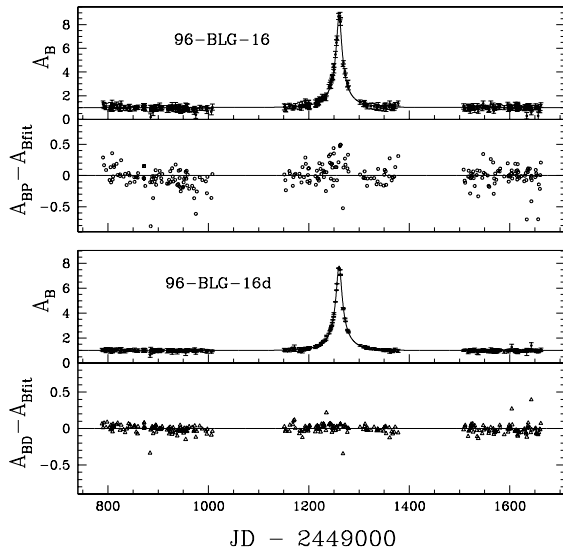


Fig. 7.— This figure shows the light curves for microlensing event 96-BLG-16. The top two panels are the standard macho blue ( $B_m$ ) and red ( $R_m$ ) PSF photometry and microlensing fit residuals. The bottom two panels are the DIA photometry and residuals for the same initial data. The fits vary slightly because the PSF photometry is blended and the difference image photometry is not. Further results are given in paper 2 (Alcock et al. (1999 paper2)).

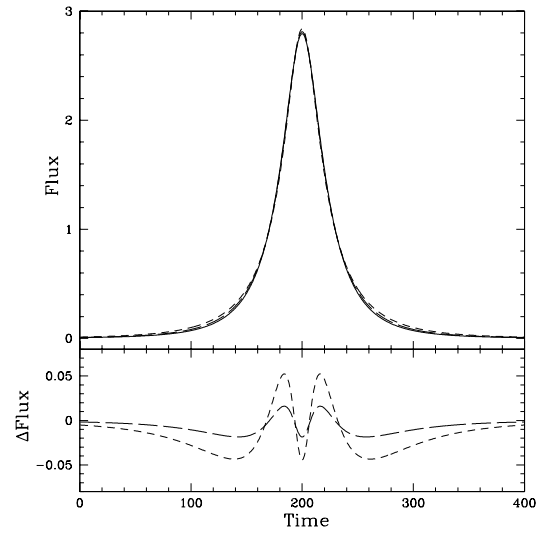


Fig. 8.— Differences between microlensing light curves for a range of source fluxes. In the top panel we show three theoretical microlensing light curves for three values of source flux. In the lower panel we show the difference between the dashed curves and the solid curve. We can readily see that, to determine the differences between these light curves and hence true source flux, we require very small uncertainties and good sampling. The parameters are given in table 1.

TABLE 1  
PARAMETERS OF MODEL EVENTS.

| $f_s$ | $A$  | $U_{min}$ | $\hat{t}$ | $t_{max}$ |
|-------|------|-----------|-----------|-----------|
| 2.0   | 2.40 | 0.448     | 85.4      | 200       |
| 1.5   | 2.87 | 0.365     | 98.0      | 200       |
| 1.0   | 3.83 | 0.268     | 120.8     | 200       |

NOTE.—Microlensing parameters for simulated events presented in figure 8.

This figure "f5a.gif" is available in "gif" format from:

<http://arxiv.org/ps/astro-ph/9903215v1>

This figure "f5b.gif" is available in "gif" format from:

<http://arxiv.org/ps/astro-ph/9903215v1>

This figure "f6a.gif" is available in "gif" format from:

<http://arxiv.org/ps/astro-ph/9903215v1>

This figure "f6b.gif" is available in "gif" format from:

<http://arxiv.org/ps/astro-ph/9903215v1>